IEEE Access
Multidisciplinary | Rapid Review | Open Access Journal

Received April 28, 2021, accepted July 3, 2021, date of publication July 12, 2021, date of current version July 21, 2021.

Digital Object Identifier 10.1109/ACCESS.2021.3096599

A Probabilistic Model and Capturing Device for Remote Simultaneous Estimation of Spectral Emissivity and Temperature of Hot Emissive Materials

ARTZAI PICON[1,2], AITOR ALVAREZ-GILA[1], JOSE ANTONIO ARTECHE[1], GABRIEL A. LÓPEZ[2], AND ASIER VICENTE[3]

[1]TECNALIA, Basque Research Technology Alliance (BRTA), Parque Tecnológico de Bizkaia, Derio, E-48160 Bizkaia, Spain
[2]University of the Basque Country UPV/EHU, 48940 Leioa, Spain
[3]Arcelor Mittal Research Centre, 48910 Sestao, Spain

Corresponding author: Asier Vicente (asier.vicente@arcelormittal.com)

This work was supported in part by the Basque Government (Hazitek AURRERA B: Advanced and Useful REdesign of CSP process for new steel gRAdes) under Grant ZE-2017/00009.

ABSTRACT Estimating the temperature of hot emissive samples (e.g. liquid slag) in the context of harsh industrial environments such as steelmaking plants is a crucial yet challenging task, which is typically addressed by means of methods that require physical contact. Current remote methods require information on the emissivity of the sample. However, the spectral emissivity is dependent on the sample composition and temperature itself, and it is hardly measurable unless under controlled laboratory procedures. In this work, we present a portable device and associated probabilistic model that can simultaneously produce quasi real-time estimates for temperature and spectral emissivity of hot samples in the [0.2, 12.0μm] range at distances of up to 20m. The model is robust against variable atmospheric conditions, and the device is presented together with a quick calibration procedure that allows for in field deployment in rough industrial environments, thus enabling in line measurements. We validate the temperature and emissivity estimates by our device against laboratory equipment under controlled conditions in the [550, 850°C] temperature range for two solid samples with well characterized spectral emissivity's: alumina ($\alpha - Al_2O_3$) and hexagonal boron nitride ($h - BN$). The analysis of the results yields Root Mean Squared Errors of 32.3°C and 5.7°C respectively, and well correlated spectral emissivity's.

INDEX TERMS Probabilistic computing, radiometry, spectral analysis, spectral emissivity, spectroscopy, steel industry, temperature measurement.

I. INTRODUCTION

The steelmaking process consists of obtaining steel products through a series of industrial steps of ferrous raw materials (scrap or iron ore) melting, liquid steel solidification and thermo-mechanical transformation. Those processes must be properly adjusted based on the features of the raw materials and the required properties of the steel products to be obtained. Currently, the two main routes for producing steel are the integrated route and electrical route [1]. However, no matter the process route used, obtaining inline detailed information, not only for steel, but also for slag in the different reactors is of vital importance for the optimization of the processes. In the digital era, in which industrial facilities tend to be automatized through process smartization, the development of online analysis tools is becoming an important topic of concern and heavy processes like EAF (Electric Arc Furnace) represent a giant challenge. In this sense, several solutions have been reported for liquid steel control in the EAF, including continuous temperature measurement by using optical fiber or optical sensors [2], dynamic metallurgical models that continuously solve mass and thermal balances for the whole system [3] or foamy slag detection by noise and arc harmonics analysis [4].

As for the EAF operation, the process begins with a mixture of different ferrous raw materials being introduced in

The associate editor coordinating the review of this manuscript and approving it for publication was Sunil Karamchandani.

the reactor. These materials are melted down in the initial phases of the procedure and then, during the steel refining phase, the liquid steel is heated up till about 1650°C. For succeeding in the steel transformation process, most of the undesired elements contained in the scrap are oxidized and moved to the slag, whose function is also to improve the efficiency of the huge amounts of energy (electrical and chemical) continuously being introduced during the EAF operation. At the end of the process, the slag is removed from the furnace and the steel is poured into a refractory ladle to be refined in the ladle furnace process.

The analysis of the slag temperature and chemical composition is of vital importance during the steel manufacturing process. The slag composition is measured manually by the use of a manually acquired and prepared sample on a spectrometer that allows calculating the steel-slag thermodynamic state. Although some automated methods have been implemented to avoid the slag sample preparation and to directly measure the slag composition based on its spectral reflectance [5], they still require the manual extraction of the slag sample, still representing a slow and manual process.

Novel methods are therefore required to measure the temperature and composition of the liquid slag without interfering with the steel manufacturing process. Currently, there exists no viable solution for accurately measuring the temperature of liquid slag, and few technologies have been posed for online understanding of slag evolution (i.e. solid/liquid fraction distribution, chemical composition or temperature) [6]. Proposing a method for remote extraction of continuous slag characteristics would allow for the optimization the EAF process by continuously adjusting the process parameters according to the evolution of the slag.

In this work, we present a novel portable spectrometer device and Bayesian probabilistic algorithm that are capable of direct remote estimation of temperature and spectral emissivity from remote radiant samples. The system captures the radiance signal incoming from an 8 cm diameter spot located up to 20 m away. A fully Bayesian model integrates all the signal pipeline, simultaneously estimating the sample temperature, spectral emissivity's, the absorption caused by the presence of water vapour and CO_2 along the optical path that explains the observed radiance with a maximum likelihood. The proposed method was validated with alumina ($\alpha - Al_2O_3$) and hexagonal boron nitride ($h - BN$) samples and compared with standard laboratory analysis obtaining good correlation. The proposed system and methods can be used in steel factory settings for in-situ electric arc furnace monitoring without the need for active thermocouple or calibration blackbody.

II. RELATED WORK

On the EAF process, temperature is a key factor that regulates thermo-chemical processes in order to yield appropriate properties of the resulting steel [3], [7]. On the other hand, slag composition determines the thermodynamic system status between the steel and slag [5]. In this sense, coming to the idea of developing methods for characterizing materials involved in the steel manufacturing process, a compact and portable device that remotely provides reliable composition and temperature values under actual industrial conditions is desirable.

The thermal infrarred range has been widely analysed by different authors in order to establish relationships between the spectral emissivity and the different materials. Different works [8]–[13] analyse the relationship between the temperature and the emissivity of different materials, evidencing the dependency of the spectral emissivity on the chemical composition for slag materials such as SiO_2, Al_2O_3, FeO, Fe_2O_3, CaO and MgO.

Temperature measurement devices are commonly divided in two different categories: those that require contact (thermometers, thermocouples, thermistors, etc.) and those that do not (e.g. pyrometers, thermographic cameras). The latter, which sense and measure the incoming infrared radiation in order to estimate the temperature, are frequently used for monitoring high-temperature furnaces. To make an accurate temperature measurement, these methods require precise knowledge on how the emissivity behaves in the spectral range that the radiation is detected, as $T = T(\varepsilon(\lambda))$. The emissivity $\varepsilon(\lambda)$ is a parameter that indicates how a material emits radiation when compared to a black body, the perfect emitter.

A number of works have proposed novel methodologies to measure emissivity and temperature in field with the use of non-contact and portable devices: Rego-Barcena *et al.* [14], [15] described a technique to obtain emissivity's in situ at different locations, with a portable, rugged and inexpensive device. Their method is capable of estimating a single spectral emissivity value and the average temperature by means of least-squared optimization. However, this method considers the boiler emitter as a gray body. This is not the case on the EAF furnace, as the emissivity depends on the composition of the slag-steel fraction [3], [8], [16]. As opposed to theirs, our method makes no assumption on the shape of the underlying spectral emissivity of the sample.

Other methods focus on estimating spectral emissivity's under controlled conditions, where the temperature is not estimated but used as a model input [9]. More recently, different Bayesian methods have been employed to model the complex interactions between the radiative physical processes: [17] used Montecarlo techniques to simulate the radiative heat transfer between surfaces, while a few works [18]–[20] apply Bayesian approaches to address the composition estimation problem.

Temperature Emissivity Separation (TES) methods aim to simultaneously estimate sample temperature and emissivity. Given the inherently under-constrained nature of the problem, most of them tackle the task by imposing certain strong priors on the proposed models [21]–[27]. A few others claim to avoid making such heavy assumptions by instead imposing a maximization of the entropy [28]–[30], although still require to explictly select the temperature and emissivity ranges within which the solution is expected to be.

Besides, in practice, these solutions are often tied in some way to the specific use case for which they were conceived. Many of the aforementioned approaches were indeed proposed and tested in the context of remote sensing applications, and thus operate under a very constrained range of plausible temperature values [21], [28].

Some of these approaches have also been applied in steel manufacturing processes. Sonoda *et al.* [31] e.g. propose a bootstrap filter-based method to estimate the probability distribution of liquid steel temperature. Meanwhile, only machine learning methods have been proposed for the estimation of the slag parameters [32].

In this work we introduce a compact and portable device that remotely produces reliable temperature and visible-IR spectral emissivity estimates under actual industrial conditions in quasi real time. The device comprises three punctual spectrometers with partially overlapping spectral ranges, covering a combined range of $[0.2, 12.0\mu m]$ for an improved predictive performance. Along with it, we present and validate a fully Bayesian radiative transfer model that seamlessly estimates and accounts for the spectral emissivity, the sample temperature and the different unknown variables that may affect the received radiance on real industrial situations such as presence of gases on the optical path or fiber misalignments on the spectrometers. It does so by leveraging the signal received by the three available spectrometers, and could easily generalize to an arbitrary number of them. As opposed to machine learning-based approaches, the model can be considered unsupervised once the calibration procedure has been completed, as it requires no further training data. In addition, it yields full density estimates of the considered random variables, thus considering the uncertainty associated to each prediction. This is possible due to its Bayesian nature, which also implies the need to impose a prior distributions over each of the target random variables. The distributions proposed in section IV-B for such priors provide a good parametrization for the very wide range of temperatures considered in this work. However, these are soft constraints that may be further softened by substituting them by other less informative distributions (or hardened, should the user wish to apply it in more constrained setups); the described framework would still be valid in both cases, and the influence of the prior distributions is in any case overridden as the evidence provided by the captured observations becomes more prevalent.

III. DESIGN OF THE DEVICE

As mentioned in section II, several systems have been proposed to simultaneously calculate spectral emissivity and temperature of hot emissive samples. However, these systems have been designed to work under strict controlled laboratory conditions and are not capable of estimating the temperature and spectral emissivity under real industrial conditions. The targeted goal for our device is to allow operating on the proximity of the electric arc furnace from the steel factory. These conditions imply high temperature, dirtiness, tolerance to mechanical impacts and vibrations and uncontrolled vapour conditions.

Based on preliminary laboratory testing and analysis, the following system requirements were defined and set as design guidelines. (i) As for the optical requirements, a spectral range of 200−12 000 nm was defined with a minimum spectral resolution of 50 nm/pixel on the far infrared region. (ii) The device should allow for the remote acquisition of a spot with a diameter of 12 mm at a distance of 20 m. (iii) The system should be able to perform simultaneous spatial and temporal acquisition, (iv) with a minimum acquisition rate of 0.5 samples per second. (v) Regarding usability, the device should provide in-field pointing capabilities and on-field calibration mechanism without the need for sending the system to laboratory for calibration. (vi) Finally, as for the working conditions, the system should be tolerant to heat and vibrations and (vii) agnostic to the presence of water vapour, CO and CO_2 on the optical path. The present work describes how a prototype fulfilling these requirements has been designed, built, calibrated ant tested both in laboratory and in real industrial conditions at the ArcelorMittal research casting factory of Sestao.

A. SYSTEM DESCRIPTION

Fig. 1 shows the acquisition device diagram. In order to capture the radiance from a 12 mm diameter area from region *(A)* located up to a distance of 20 m we employ a UV-Enhanced Aluminum Reflective collimator *(B)* with an SMA connector that assures a 12 mm beam and a good reflectivity throughout the required range. The captured radiance passes through a special fiber *(C)* comprising a fiber bundle that ends in 4 SMA-905 outputs *(D)*. This fiber bundle is composed by one input and four outputs, allowing spectral coverage in the 200−12 000 nm range. This fiber bundle is composed by seven fibers: 1×200 µm UV-VIS fiber, 3×240 µm Polycristaline infrared (PIR) fibers and 4× VIS-NIR 200 µm fibers. Two VIS-NIR fibers *(H)* are connected to an inline splice bushing connector (Thorlabs 20-02) *(I)* which is also connected to a green laser source *(J)* (MGL-III-532-300 mW) that serves as system pointer. The UV-VIs fiber *(E)* connects into a UV-VIS spectrometer *(L)*, an Ocean Optics HR2000 with a composite grating covering 200−1100 nm. A notch filter *(K)* (Thorlabs NF533-17) is placed to remove green laser signal from the spectrometer entrance. The other two VIS-NIR fibers *(F)* are connected to a Fourier transform infrared spectrometer *(M)* composed by a *CaF* beamsplitter, with an *InGaAs* detector covering the 0.9−2.6 µm range (ArcOptics). The two PIR fibers are connected to a second Fourier Transform Infrared spectrometer *(N)* with a *ZnSe* beamsplitter covering the 2.5−12 µm range (ArcOptics).

The system is packed into an acquisition case (see Fig. 2) that allows taking measurements on industrial conditions. The case provides mechanical protection to the optical components as well as data connectivity based on a single USB output connection for all the different acquisition devices.

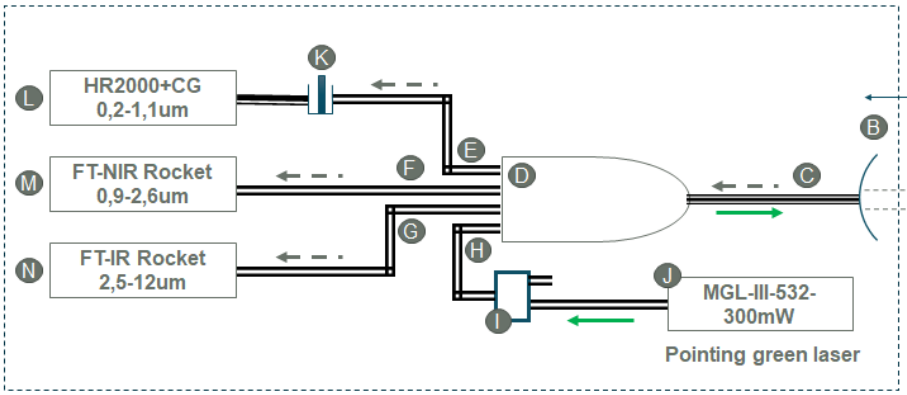

FIGURE 1. Design diagram of the acquisition system. Targeted point is illuminated by the green laser (J). A collimator (B) captures the signal, which is transmitted to the three spectrometers (L), (M) and (N) through the fiber bundle (D). Filter (K) eliminates the signal from the green laser (J).

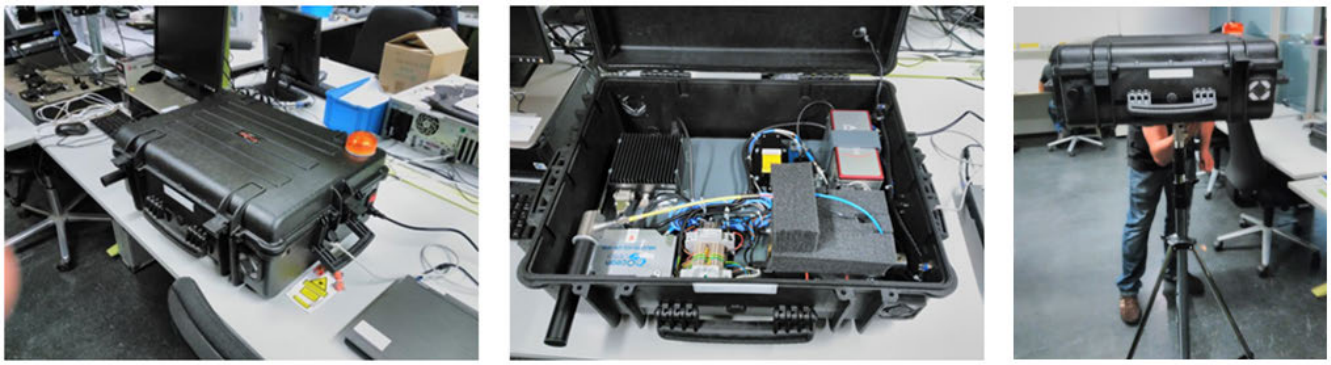

FIGURE 2. Packed prototype. (left) Acquisition case, (middle) Packed opto-mechanical system, (right) Tripod mounting.

In order to obtain a continuous spectral signature in each capture, a dedicated software has been developed. The software performs real time acquisition of the data from the three spectrometers and it applies the latest optical system's calibration function on the fly. It allows plotting, recording and saving the captured information, and provides access to the specific low-level settings of each independent spectrometer.

B. SYSTEM CALIBRATION

The calibration of the system have been divided into two different processes. A first process models the spectrometers' non linear response and generates the optical system transfer function. However, the intended working conditions of the system may significantly affect the system calibration. Fiber re-installation, vibrations and in-place temperature variations affect the amount of radiance acquired by each spectrometer. This makes necessary an additional in-situ calibration of the system. To cope with this, a second calibration stage based on a stabilized calibration lamp is added to the system operation.

1) CALIBRATION OF THE NON-LINEARITIES OF THE SPECTROMETERS

Each spectrometer wavelength was calibrated by fitting a 2^{nd} degree polynomial function that maps the collected counts by the spectrometer at each λ_i into the theoretical blackbody radiance at the blackbody temperature (T_j). The polynomial coefficients W_{λ_i} are estimated at each wavelength λ_i by minimizing the root mean square error between the theoretical blackbody emissivity at T_j: $L_{bb_{\lambda_i}}(T_j)$ and the mapping of the counts $C_{\lambda_i}(T_j)$ acquired by the spectrometer when looking into a calibrated blackbody at temperature T_i at λ_i as described in (1):

$$\arg\min_{W_{\lambda_i}} \sqrt{\sum_{T_j=T_0}^{T_n} [L_{bb_{\lambda_i}}(T_j) - f_{calib}(C_{\lambda_i}(T_j), W_{\lambda_i})]^2} \quad (1)$$

where f_{calib} is a 2^{nd} degree polynomial function that takes W_{λ_i} as its polynomial coefficients to map spectrometer acquired counts into theoretical radiance.

To calibrate the system, acquisitions over a blackbody furnace between 500°C and 1500°C were performed at the closest possible distance of 600 mm from the tip of our system collimator and the end of the blackbody furnace. Fig. 3 depicts the calibration setup. It is noteworthy to remark that this optical path contained gases composition that corresponds to the part of the atmospheric transmittance corresponding to the optical path that is inside of the calibrated device. However, this effect can be considered negligible in comparison to the full optical path.

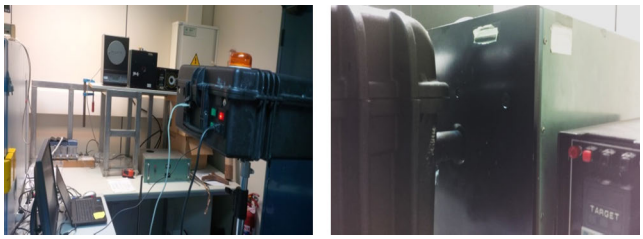

FIGURE 3. Acquisition system under calibration set-up.left) System on the calibration room close to the blackbody furnace, right) Close-up.

The root mean squared error resulting from this process was 2% for spectrometer 1 (200−1100 nm), 1% for spectrometer 2 (970−2600 nm) and 0.5% for spectrometer 3 (2500−12 000 nm), as illustrated in Table 1. Correlation among theoretical radiance and calibration-corrected captured samples for three specific wavelengths and six temperatures is depicted in Fig. 4.

TABLE 1. Acquisition system calibration error (%).

Calibration distance (mm)	Test distance (mm)	Spectrometer	RMSE (%)
1000	1700	1	2%
1000	1700	2	1%
1000	1700	3	0.5%

2) FIELD CALIBRATION

Working in industrial conditions makes the system be affected by mechanical vibrations, dust, temperature changes, etc. Even the movement between the different fibers occasionally led to observed intensity changes of up to 15% on the collected signal. Fortunately, these changes are related to the coefficient of transmission between the different fibers and devices. We model this transmission coefficient as independent from wavelength. Based on this hypothesis, we assume that the change in the amount of radiance acquired by each spectrometer S can be modelled by a proportional factor C_s that does not depend on the wavelength.

In order to reduce this effect, a stabilized spectral calibration lamp emulating a blackbody at 1500 K (Thorlabs SLS203L (500−9000 nm)) is proposed for daily calibration at the beginning and at the end of each acquisition campaign. The calibration lamp is used with an installed diffusion filter to allow for diffuse illumination into the collimator. Fig. 5 depicts the imaging system with the coupled calibration camera.

The field calibration procedure is defined as follows: (i) During the spectrometers' non-linearity calibration phase (section III-B1) the calibration lamp is mounted into the system and switched on, and the radiance captured by the different spectrometers $L_{s0}(\lambda)$ is stored as reference. (ii) Later, during the field measurements, the calibration lamp is set again and the new signal $L_{s1}(\lambda)$ is recorded. (iii) For each spectrometer, the ratio of the average intensity between the two lamp signals along a specific spectral range $[\lambda_l, \lambda_h]$ is used for signal correction, as shown in (2). An spectral range of 450−900 nm is used for spectrometer 1, 960−2500 nm for spectrometer 2 and 3500−4000 nm for spectrometer 3. Figure 6 shows the resulting three obtained correction factors K_s, one per spectrometer. The RMSE before correction was 11% for the signal induced by the calibration lamp, whereas this error was reduced to 0.4% after applying the correction factors.

$$K_s = \frac{\sum_{\lambda=\lambda_l}^{\lambda_h} L_{s1}(\lambda)}{\sum_{\lambda=\lambda_l}^{\lambda_h} L_{s0}(\lambda)}, \quad \forall s \in \{1, 2, 3\} \tag{2}$$

IV. RADIATIVE TRANSFER MODEL

A. MODEL FORMULATION

Our final aim is the simultaneous estimation of the temperature T_{bb} and spectral emissivity $\varepsilon(\lambda, T_{bb})$ of the observed hot sample, taking as sole input the number of counts (i.e. digital level magnitude) yielded by the capture software as a function of the wavelength, $C(\lambda)$. We model the scenario described in the preceding sections as a perfect blackbody radiator $L_{bb}(\lambda, T_{bb})$ emitting at our unknown target temperature T_{bb}, whose emission is successively filtered by (i) a selective filter with a transfer function that equals the spectral emissivity that characterizes the sample (both conforming a selective radiator), (ii) the atmospheric spectral transmittance of the optical path between the device and the sample, $\mathcal{T}_{atm}(\lambda)$, and (iii) the transfer function of the full multi-spectrometer optical system, $\mathcal{T}_{OS}(\lambda)$ (comprising the fibers, optical components, detector and the slit function modelling its spectral convolution), which is determined by the calibration process (see section III), and relates the observed physical magnitude -radiance, in $W/m^2\mu m$- to the counts yielded by each of the spectrometers. Equation (3) formalizes this model, which is graphically described in Fig.7 [33].

$$C(\lambda) = \mathcal{T}_{OS}\left[L_{bb}(\lambda, T_{bb}) \cdot \varepsilon(\lambda, T_{bb}) \cdot \mathcal{T}_{atm}(\lambda)\right] \tag{3}$$

Thus, the calibrated radiance being observed by our system, $L_{obs}(\lambda)$ can be obtained by inverting the precomputed optical system's transfer function (resulting from the calibration process described in section III-B) and directly applying it to each captured observation:

$$L_{obs}(\lambda) = \mathcal{T}_{OS}^{-1}\left[\mathcal{T}_{OS}\left(L_{bb}(\lambda, T_{bb}) \cdot \varepsilon(\lambda, T_{bb}) \cdot \mathcal{T}_{atm}(\lambda)\right)\right] \tag{4}$$

The remaining terms in (4) contain certain variables that are either our target magnitudes (i.e. spectral emissivity, $\varepsilon(\lambda, T_{bb})$ and temperature T_{bb} of the equivalent ideal blackbody) or side parameters that need to be estimated from our observations. In order to solve for these all simultaneously we adopt a probabilistic programming framework and build a Markov-Chain Monte Carlo (MCMC) based Bayesian inference model. The modeling details of each of such terms are introduced in the rest of this section:

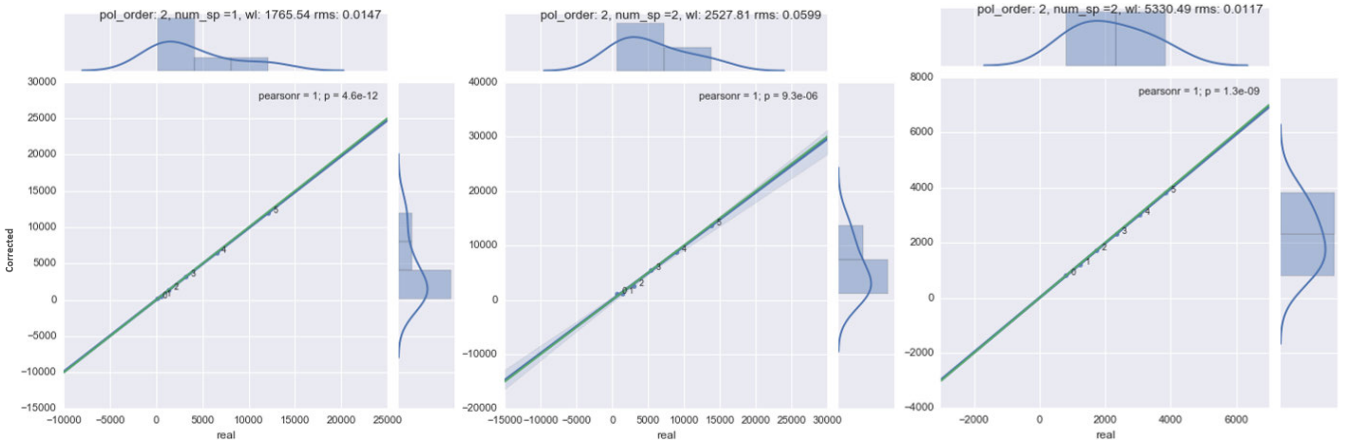

FIGURE 4. Correlation plot of the calibrated system response vs. an ideal blackbody source for three separate wavelengths (1765.54 nm, 2527.81 nm, 5330.49 nm) at six different furnace temperatures. x axis: theoretical blackbody radiance at the specific wavelength. y axis: radiance estimated by the calibration polynomial.

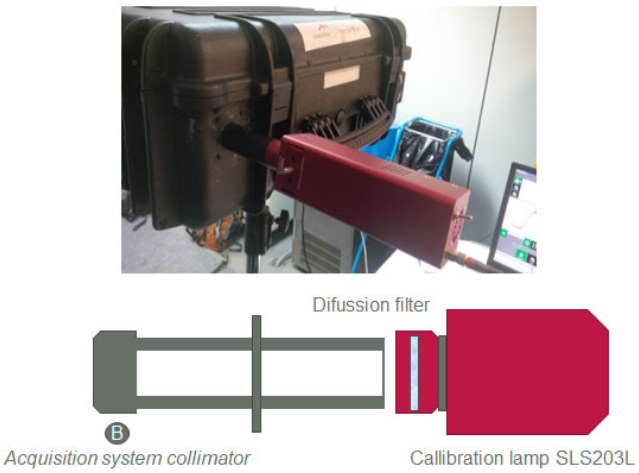

FIGURE 5. Calibration lamp for field calibration. (left) System mounted for calibration, (right) Lamp calibration diagram: calibration lamp, diffusion filter and SLS203L camera.

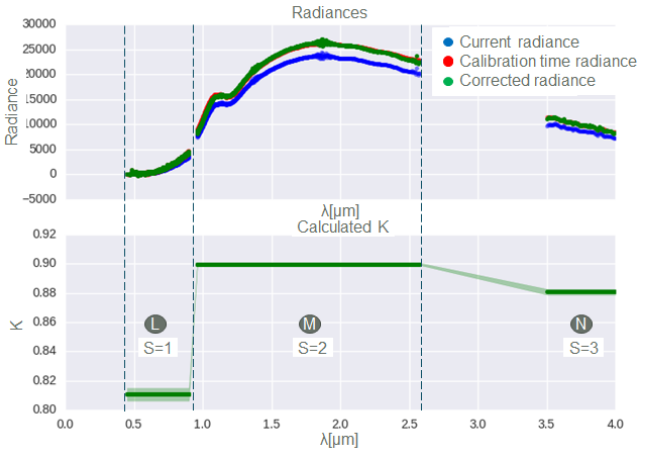

FIGURE 6. Calibration correction by using the calibration lamp. (top) In blue, the current radiance received by the sensor, in red the reference radiance obtained at calibration time and in green the corrected radiance after applying the correction factors K_S. (bottom) The three K_S correction factors calculated, following (2), as the ratio of current collected collected lamp-induced radiance $L_{s1}(\lambda)$ and the radiance collected with the lamp right after the nonlinear response calibration $L_{s0}(\lambda)$.

The **ideal blackbody radiance**, $L_{bb}(\lambda, T_{bb})$, is defined as:

$$L_{bb}(\lambda, T_{bb}) = \frac{2hc^2}{\lambda^5} \frac{1}{e^{\frac{hc}{\lambda k_B T_{bb}}} - 1} \tag{5}$$

where k_B is the Boltzmann constant, h is the Planck constant, and c is the speed of light. Equation (5) shows the heavy dependence of the radiance $L_{bb}(\lambda, T_{bb})$ with the target temperature T_{bb} of the sample. An accurate estimation of this parameter is thus critical. We consider such temperature a stochastic variable to be estimated by the probabilistic model.

The **spectral atmospheric transmittance**, $\mathcal{T}_{atm}(\lambda)$, can be defined as a function of the distance, d, between the capturing device and the observed radiating sample, and the attenuation coefficient of the atmosphere, γ_{atm}. The latter can be further decomposed in terms of the molar concentration x and the unitary absorption coefficient γ of each of the considered absorbents, a. Therefore:

$$\mathcal{T}_{atm}(\lambda) = e^{-d \cdot \gamma_{atm}} = e^{-d \cdot \sum_a -x_a \cdot \gamma_a} \tag{6}$$

The distance d is set manually according to the acquisition set-up, while the attenuation coefficients are obtained from the HITRAN2016 (High Resolution Transmittance) molecular spectroscopic database [34], which comprises spectroscopic parameters for a number of gaseous molecules with a high spectral resolution, and constitutes the *de facto* standard for the simulation of atmospheric molecular absorption under arbitrary conditions. The HITRAN Application Programming Interface (HAPI) [35] was used during this work in order to obtain accurate and line-by-line information about the absorbents being considered in our measurements. HAPI provides the molecule-specific attenuation coefficient infor-

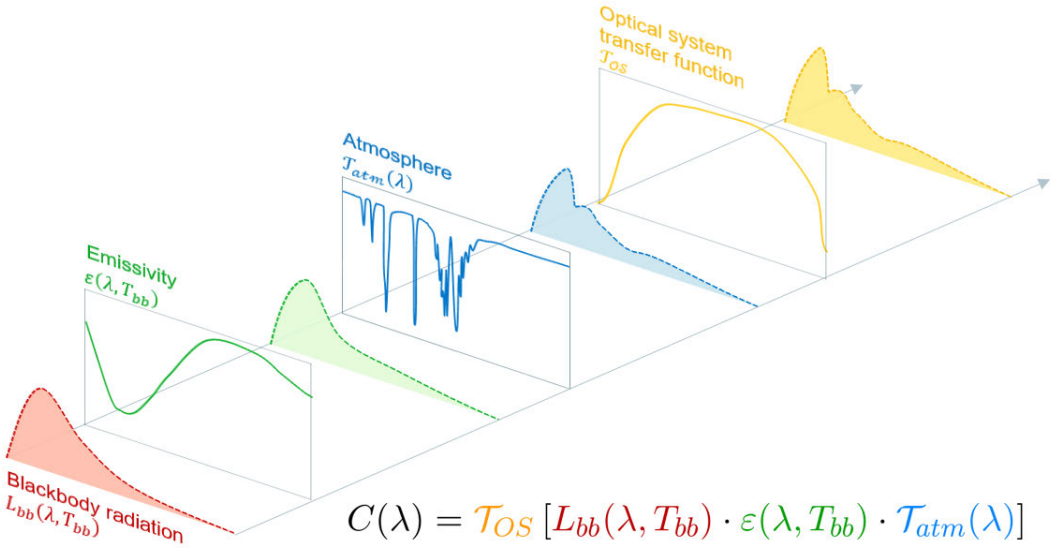

FIGURE 7. Radiative transfer model: The radiance from a blackbody emitter at the unknown sample temperature is successively filtered by the spectral emissivity of the sample, atmospheric transmittance of the optical path, and transfer function of the capturing optical system and sensor. The model is solved through Bayesian probabilistic inference and yields full probability density estimates of sample temperature, spectral emissivity, atmospheric CO_2 and H_2O concentrations, and other auxiliary variables. Dashed lines represent signals, continuous lines represent the different steps modeled by their spectral transmittance.

mation in the form of cross section (σ_i) with $[cm^2/molecule]$ units, which we then convert appropriately. In our case, the molar concentration of the absorbents (x_a) are unknown probabilistic variables to be estimated by the model. We initially considered a set of potentially significant absorbents comprising $H_2O, CO_2, O_3, CO, CH_4, N_2O$, and O_2. However, after simulating the spectral atmospheric transmittance due to each of them within a range of typical concentrations, sampling distances and ambient conditions in industrial environments (see Fig. 8), only H_2O, CO_2 where kept in the model as the ones with non-negligible contributions to the overall absorbance, in order to reduce potential sources of overfitting. Hence, (6) can be further decomposed:

$$\mathcal{T}_{atm}(\lambda) = e^{-d\cdot\gamma_{atm}} = e^{-d\cdot(x_{CO_2}\cdot\gamma_{CO_2}+x_{H_2O}\cdot\gamma_{H_2O})} \tag{7}$$

Fig. 9 shows the effect of the resulting typical atmospheric transmittance over the emission of an ideal blackbody at 1550 °C at a sampling distance of 1.5 m .

The definition domain of the **spectral emissivity**, $\varepsilon(\lambda, T_{bb})$, of the observed radiative source -our main target variable, which is continuous as a physical magnitude- is given by those of the three spectrometers of the capturing device, which, together, sample the continuous spectrum at $\lambda_i\ \exists\forall i \in [1, N]$.

However, in order to prevent overfitting, we regularize the spectral emissivity with a set of M probabilistic variables ε_k, with $k = 1, \ldots M$ and $M \ll N$, each paired with one specific anchor wavelength in the considered range, and whose values represent the value of the spectral emissivity of the radiative source at each of such spectral sampling points.

In order to obtain the spectral emissivity defined for every value of λ_i, we take advantage of the smooth variation of the spectral emissivity function [36], and pose M fuzzy sets defined by their triangular membership functions μ_k:

$$\mu_k(\lambda) = \begin{cases} 1 - \left|\dfrac{\lambda - \lambda_{ck}}{D}\right| & \lambda_{ck} - D < \lambda < \lambda_{ck} + D \\ 0 & \text{otherwise} \end{cases} \tag{8}$$

where λ_{ck} is the central wavelength corresponding to $\varepsilon_k, \forall k \in [1, \ldots M]$. Using this representation, the spectral emissivity at any arbitrary wavelength i can be estimated as the weighted value of the peak emissivity values, ε_k, defined at the center of the each fuzzy set (Fig. 10).

Multi-spectrometer setup Although useful for standalone-spectrometers, the presented model does not take into account the case where the observed spectral radiance signal is a combination of a set of various spectrometers operating in adjacent, partially overlapping regions of the spectrum. Regions perfomning high noise were removed from the model. For spectrometer 1 wavelengths between $0.2-0.4\ um$ and $0.9 - 1.2\ um$ were removed due to spectrometer lack of sensitivity. For spectrometer 2, wavelengths between $2.5 - 2.7\ um$ were removed and for spectrometer 3, wavelengths between $1.6 - 3.0\ um$ and were removed. The optical system of our device comprises, though, three different spectrometers, six bunches of optic fiber and a reflective collimator, whose aperture causes that the three spectrometers do not measure exactly the same area. In order to account for this and for possible fiber misalignments, we introduce a set of three additional proportionality correction probabilistic

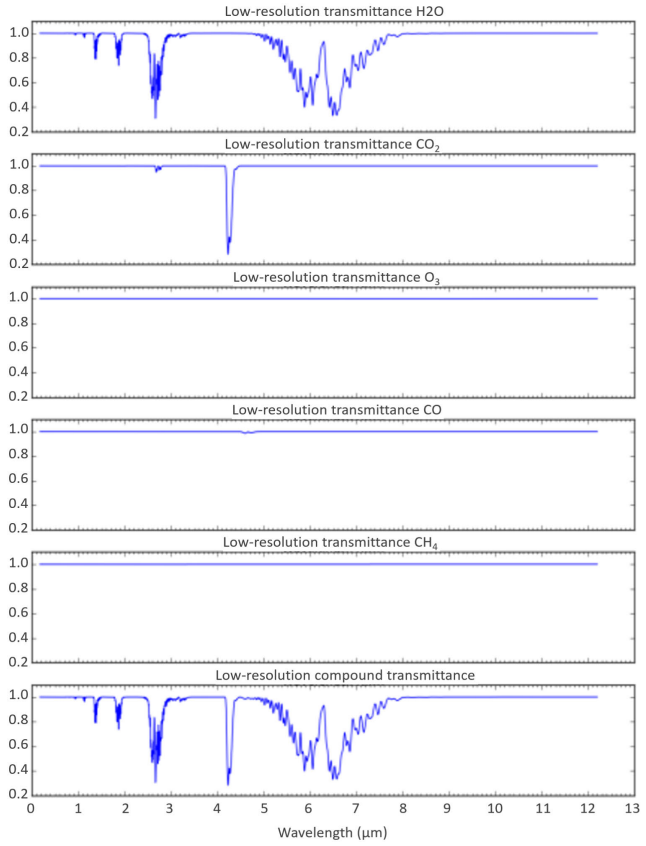

FIGURE 8. Spectral atmospheric transmittance due to each of the considered absorbents (H_2O, CO_2, O_3, CO, CH_4, N_2O, and O_2.) and the combined transmittance for typical concentrations and 27°C, at a distance of 1.5 m.

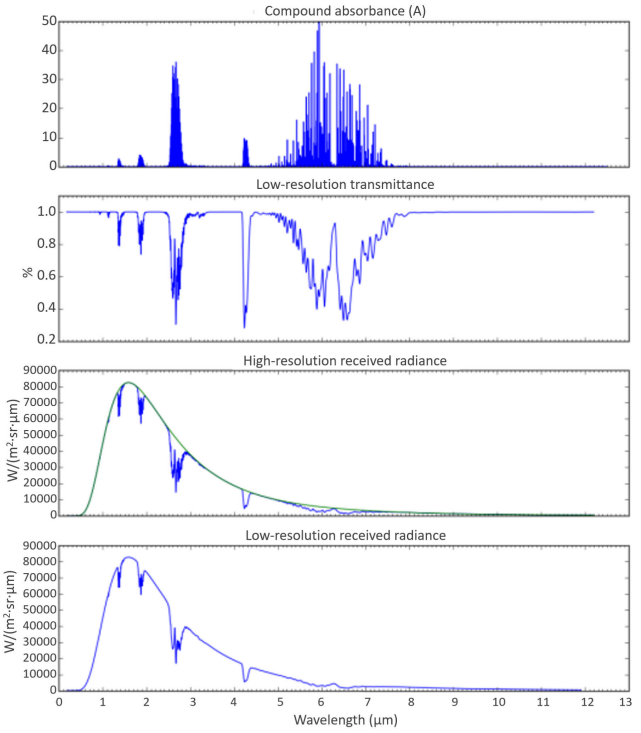

FIGURE 9. Radiance from an ideal blackbody at 1550°C filtered by simulated atmospheric transmittance due to H_2O, CO_2 absorption at typical concentrations and 27°C, sampled at distance of 1.5 m. 1st row) Combined absorbance of the optical path at high spectral resolution, as yielded by the HAPI model (i.e. line-by-line cross-section information). 2nd row) Equivalent transmittance as a result of converting the original, line-by-line magnitude to a low resolution one -matching those of the spectrometers- by convolving the signal with the slit function that characterizes each of the spectrometers' sampling processes (a *sinc* function for the FTIR spectrometers and a triangular function for the non-FTIR one). 3rd row) Blackbody radiance and high resolution radiance once filtered by the atmosphere. 4rd row) Atmosphere-filtered radiance convolved and downsampled to match the spectrometers' resolution.

variables k_s (with $s = 1, 2, 3$) into the model. These are constant for every value of λ within each spectrometer, and their prior value can be pre-calculated by the use of a calibration lamp as shown in (2) and explained in section III-B2. Minor variations over the pre-computed K_s can be estimated by the model should they provide a better explanation (i.e. higher likelihood) of the observed data.

The resulting radiative transfer model is thus:

$$L_{obs}(\lambda) = \mathcal{T}_{OS}^{-1}\left[\mathcal{T}_{OS}\left(k_s \cdot e^{-\gamma_{atm}(\lambda)\cdot d}\cdot\varepsilon(\lambda, T_{bb})\cdot L_{bb}(\lambda, T_{bb})\right)\right] \quad (9)$$

which contains $M + 6$ unknown parameters that need to be estimated, i.e. $\theta = \{T_{bb}, \sigma, x_{CO_2}, x_{H_2O}, k_1, k_2, k_3, \varepsilon_k\}\ \forall k \in [1 \ldots M]$. T_{bb} was directly one of our ultimate targets, and the other one, i.e. $\varepsilon(\lambda, T_{bb})$, can then be reconstructed for every value of $\lambda_i\ \forall i \in [1 \ldots N]$ via the membership functions (μ_k) from $\varepsilon_k\ \forall k \in [1 \ldots M]$.

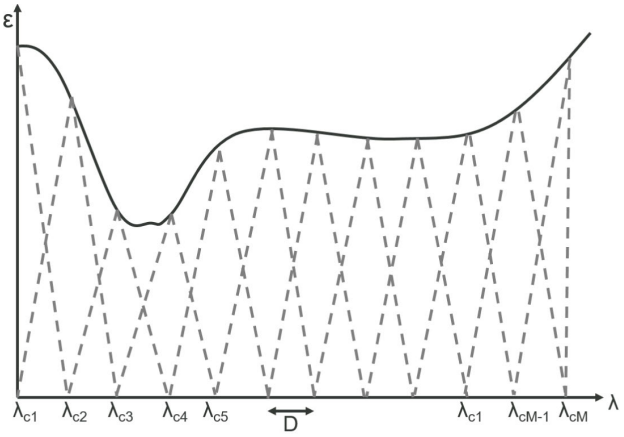

FIGURE 10. Triangular shaped membership functions μ_k, defined over their respective M central wavelengths λ_{ck}, $k = 1 \ldots M$ and with a distance D between adjacent central wavelengths λ_{ck}.

B. SOLVING THE MODEL THROUGH PROBABILISTIC INFERENCE

The only information available to estimate these unknown variables are the observations acquired by the capturing device, L_{obs}, and the radiative transfer model defined by (9). In order to do so, a probabilistic Bayesian inference approach is proposed. The field of Bayesian inference addresses the classical problem of fitting a probabilistic parametric model —our equation (9)— to the available noisy observations, i.e. learning the values of the model parameters, θ,

that best explain the measured data, assuming that the model describes the data generation process faithfully. As opposed to well-known point estimators for such parameters (e.g. Maximum Likelihood, or Maximum A Posteriori), Bayesian inference constructs a full probability distribution over the values of each model parameter, in such a way that we gain insight about the goodness of our fit, effectively modeling the inherent uncertainty of any measurement process and accounting for the fact that there is no single optimal set of parameter values which are compatible with the noisy observations.

At the core of this approach lays the classical Bayes' formula:

$$P(\theta \mid x) = \frac{P(x \mid \theta)P(\theta)}{P(x)} \tag{10}$$

where:

- $P(\theta \mid x)$, known as the *posterior probability distribution*, is the probability of each parameter value given the measured data. This is ultimately our quantity of interest, the one we need to compute.
  In this case we have:

$$P(\theta \mid x) = P(T_{bb}, \sigma, x_{CO_2}, x_{H_2O}, k_1, k_2, k_3, \varepsilon_1, \ldots \varepsilon_M \mid L_{obs}(\lambda)) \tag{11}$$

  and we are ultimately willing to know what are the sample temperature (T_{bb}) and emissivity's $\varepsilon_k(T_{bb})$ that best explain the measured radiance data.
- $P(x \mid \theta)$ is the *likelihood*, i.e. how we think the data is distributed given a parameter set θ, or how likely it is that the data was generated by our model with such given parameter set. This is what we use to evaluate how well our model explains the data, and where we describe how our data was generated, guided by (9).
- $P(\theta)$ is the *prior*, i.e. the probability distribution over the different parameter values. This is the magnitude that we can use to incorporate any prior knowledge we could have over the parameter values. Table 2 summarizes the prior assignments used in our solution.
- $P(x)$ is the *evidence* that the data was generated by this model, which could be computed by integrating over all possible parameter values: $P(x) = \int_\theta P(x, \theta) d\theta$. For non-trivial models, though, we are not able to compute this integral in a closed form.

The intractability of $P(x)$ makes the exact computation of $P(\theta \mid x)$ impossible in most of real-world examples. However, we can try to approximate the posterior making use of Markov Chain Monte Carlo (MCMC) methods, which work by constructing a Markov Chain that generates samples yielding a distribution that matches that of the posterior:

$$P(\theta \mid x) \propto P(x \mid \theta)P(\theta) \tag{12}$$

This can be achieved by defining just the priors and likelihood, thus avoiding the need to work with the evidence term. The main of the few caveats to be taken into account is that the samples from the resulting distribution are not independent i.e. there is a certain non-zero serial correlation between them, but the resulting distribution can be monitored to this respect so as to ensure a good-enough *mixture* (i.e. sampling).

The subject of probabilistic programming has recently emerged as a field that helps programmatically describe how the available data have been generated in terms of random variables, probability distributions and deterministic relations that can be used to model real-world processes. Specific programming languages exist that follow and implement this paradigm, but some general-purpose languages, such as Python, also offer library-based approaches to it, such as PyMC3 [37], which was our library of choice.

The first modeling decision was to represent the difference between the expected theoretical spectral radiance (given by the successively filtered Planck's law) and the obtained measurement as a normal distribution $\mathcal{N}(\mu, \sigma^2)$, where each sample corresponds to a given wavelength. This corresponds to our likelihood. We can thus define our observed radiance data, L_{obs}, as:

$$L_{obs} \sim \mathcal{N}(\mu, \sigma^2) \tag{13}$$

where the expected value of the distribution, μ, around which the measured samples are expected to be located, follows a deterministic transformation of the random variables according to (9):

$$\mu = L_{expected}(\lambda) \tag{14}$$

And the standard deviation of the distribution is also a random variable with a prior following a Half-Cauchy distribution [38] with a fixed *beta* parameter value:

$$\sigma \sim HalfCauchy(\beta = 10) \tag{15}$$

This means that we are assigning high likelihoods to those unknown random variables that generate a theoretical $L_{expected}(\lambda)$ radiance which is numerically close to the $L_{observed}(\lambda)$ radiance acquired by our device. MCMC obtains the posterior probability $P(\theta \mid x)$ by sampling from some probability distributions that represent our prior knowledge over each of the unknown model parameters from the model independently of the observed data. We define such parametrized prior distributions in Table 2, by observing their expected occurrence in nature:

- T_{bb} is the expected temperature distribution of the target sample. We use the minimum and maximum temperature values and set a uniform distribution between those values.
- The values of the molar concentrations of CO_2 and H_2O are based on real typical atmospheric ranges.
- K_s are pre-calculated with a calibration lamp as defined in (2) (section III-B2) and the model assumes that there can be some variation over this pre-calculation. Consequently, they are modeled as normal variables.
- ε_k is the expected value of the spectral emissivity of the radiative source at the k^{th} control wavelength.

TABLE 2. Prior distributions assigned to each of the random variables from our Radiative Transfer Model from (9).

Parameter	Name	Prior distribution
T_{bb}	Sample temperature	$\sim \mathcal{U}(min = 400°C, max = 1500°C)$
x_{CO_2}	Molar concentration of CO_2	$\sim \mathcal{N}(\mu = 450ppm, \sigma^2 = 50^2)$
x_{H_2O}	Molar concentration of H_2O	$\sim \mathcal{N}(\mu = 36000ppm, \sigma^2 = 500^2)$
k_s	Spectrometer-wise misalignment proportionality constant	$\sim \mathcal{N}(\mu = [\text{closed form } K_s, \text{eq. } 2], \sigma^2 = 0.001^2)$
ε_k	Spectral emissivity anchor value	$\sim \mathcal{U}(min = 0.0, max = 1.0)$
L_{obs}	Observed radiance	$\sim \mathcal{N}(\mu = [\text{closed form, eq. } 9], \sigma^2)$
σ	Standard deviation of the $\mathcal{N}$ modeling L_{obs}	$\sim HalfCauchy(\beta = 10)$

- σ models the intensity of the noise existing on the captured signal, independently of the region of the spectrum where it is produced. The extremes of the spectral range of each of the spectrometers are more prone to larger noise levels, while central wavelengths of the respective ranges exhibit less noise. The imposed Half-Cauchy distribution (15) aims at modeling such behavior.

Once we have described the observed data generation process (atmosphere-corrected and calibrated radiance as given by the spectrometers), we can apply MCMC to obtain samples from the posterior distribution of each of the unknown variables. Note that, as a result, we will have simultaneous probabilistic estimates for all the random variables that we defined along this description. These will be our model parameters:

$$\theta = \left\{T_{bb}, \sigma, x_{CO_2}, x_{H_2O}, k_1, k_2, k_3, \varepsilon_1, \ldots \varepsilon_M\right\} \quad (16)$$

In reality, MCMC comprises a full family of distinct algorithms for generating such samples. One of the most efficient ones in the task of going over the full multidimensional posterior space generating samples is the NUTS (No-U-Turn Sampler) sampler [39], used in our solution, which takes advantage of the use of the gradient for such duty. In doing so, the more data samples we have, the lower will the uncertainty in the parameter estimation be, and the less the serial correlation of the samples. This will be reflected in narrower monomodal distributions for these estimates. Also, for the same sample size, the uncertainty will grow as the number of parameters we need to estimate increases.

In summary, a complete Bayesian probabilistic model was built, which is sensitive to both the observed data and the theoretical framework comprising the optical calibration transfer function of the device, the proportional misalignment and calibration correction factor of the individual spectrometers, the spectral emissivity and temperature of the radiative sample, and the atmospheric absorption corresponding to the optical path between the device and the observed sample. The joint modeling of these parameters by means of a Bayesian inference model implemented via probabilistic programming makes the developed model remarkably flexible and robust, and enables the simultaneous estimation of all the unknown parameters.

V. EXPERIMENTAL VALIDATION

In order to validate the proposed method and acquisition system, two different reference materials were chosen: Alumina ($\alpha - Al_2O_3$) and hexagonal boron nitride ($h - BN$), for which the emissivity has already been studied [40]–[43]. The spectral emissivity of these materials was carefully measured in laboratory conditions using the HAIRL emissometer and applying a recently upgraded quantification methods [40], [44]. Making use of a dedicated experimental device, infrared spectral directional emissivity measurements were performed accurately in a controlled atmosphere as a function of temperature, emission angle, and *in situ* surface state evolution. These samples have been chosen for its high-temperature structural stability and the presence of a Christiansen wavelength. This is a wavelength in the infrared region that appears in certain ceramic materials at which the emissivity equals to one [41]. It is a very useful feature to obtain the sample temperature at time it is being measured. As the emitted radiation equals to $R = \varepsilon L(T, \lambda)$, where L is the Planck function, knowing the emissivity at a certain wavelength allows calculating the temperature. Since the Christiansen wavelength is temperature-independent, usually it is easily determined at room-temperature by obtaining a spectrum with an integrating sphere.

The spectral emissivity and sample temperature of both materials were estimated under factory industrial conditions by the system and methods proposed in this paper. The validation of the temperature estimation process was performed by attaching a thermocouple to the sample whereas the spectral emissivity's of the materials were compared with the values measured through the HAIRL emissometer, showing high correlation. This section details the performed experiments.

A. EXPERIMENTAL SETUP

1) LABORATORY MEASUREMENT SETUP

Normal spectral emissivity measurements were performed in laboratory air using a Fourier-transform infrared spectrometer (FTIR) with a thermal DLaTGS detector ($1.43-25\,\mu m$ spectral range, a reference blackbody (Isotech Pegasus 970-R®) and an optical entrance box that allows switching between the blackbody source and the sample chamber by a rotating plane mirror. As pointed out in [44], a 10° tilting was applied to the sample to avoid spurious signals. The sample was heated with a resistive Kanthal® wire located underneath, as depicted in Fig. 11. It was heated at a 0.4 K/s rate in order to avoid cracking from sudden thermal expansion and it was stabilized for 15 minutes to ensure high-temperature stability and constant radiance.

The emissivity measurements were performed between 100°C and 860°C. To determine the actual sample temperature, a non-contact method suitable for materials with low thermal and electrical conductivities was applied. It makes use of the so-called Christiansen wavelength, at which the emissivity is very close to 1 and almost independent of the temperature [40], [41]. The Christiansen wavelength is determined by means of a simple room-temperature reflectivity measurement using an integrating sphere. Then, each measurement temperature is computed by manually forcing

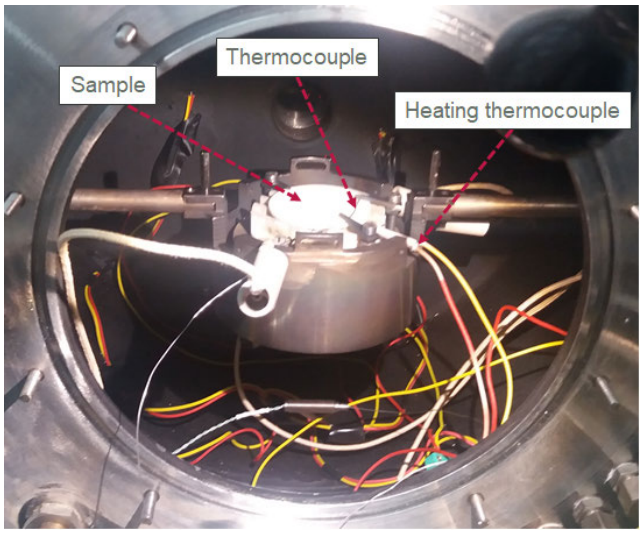

FIGURE 11. Arrangement of the sample in the analysis chamber.

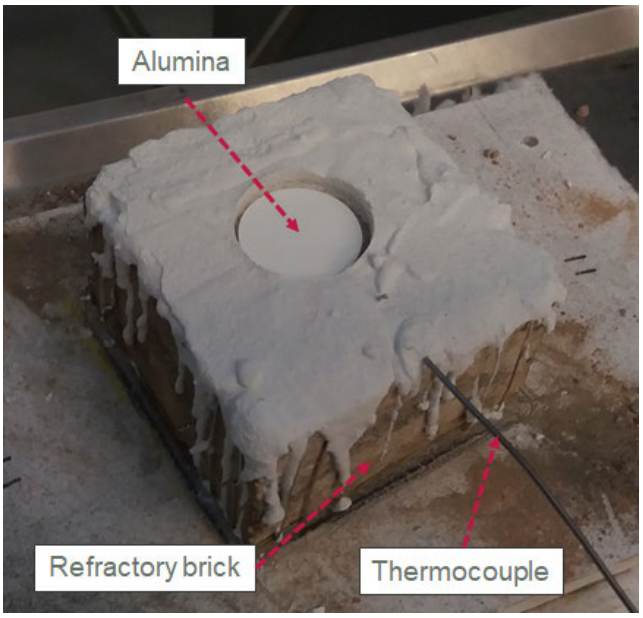

FIGURE 12. Sample holder for the alumina, including the attached thermocouple.

the emissivity at the Christiansen wavelength to be the value determined in the reflectance measurement (very close to 1).

2) IN-FIELD INDUSTRIAL SETUP

For the industrial conditions measurement, a refractory brick was used to hold the alumina sample. In order to allow time for an accurate temperature measurement, a thermocouple was attached to the sample by means of refractory cement, as depicted in Fig. 12. The calibrated acquisition system was positioned at a top position and in-situ calibration was performed following the procedure explained in section III-B2 making use of the calibration lamp.

The sample was then heated by means of a LH 15/12 Nabertherm furnace up to 1100°C. After a stabilization time of 10 min the sample was taken off the furnace and placed on the sample stage. The system was monitored simultaneously by an OPTIX PT 50 (1100−1700 nm) external pyrometer and a FLIR T640 (7500−14 000 nm) external thermal camera that were used as control devices. The experimental setup is presented in Fig. 13.

Under this configuration, the sample temperature is continuously being monitored by the thermocouple. The sample radiance was also captured by the presented multi-spectrometer device at a rate of 0.75 samples/s, with all radiance in the 200−12 000 nm being captured. The acquired signal was processed by the probabilistic algorithm detailed in section IV and the sample temperature and the spectral emissivity's at the anchor wavelengths $\lambda_{ck} = \{0.2, 1.0, 1.5, 2.0, 3.0, 5.0, 6.5, 8.0, 10.0, 12.0\}\mu m$ are estimated. The experiment was stopped when the measured sample temperature reached around 600°C, at which the radiance signal becomes too noisy for our system. This temperature corresponds, in terms of approximate equivalent radiance for the case of the two considered materials, with the lower bound of the calibration range described in III-B, which can be shown shaded in red in Fig. 17 and Fig. 23.

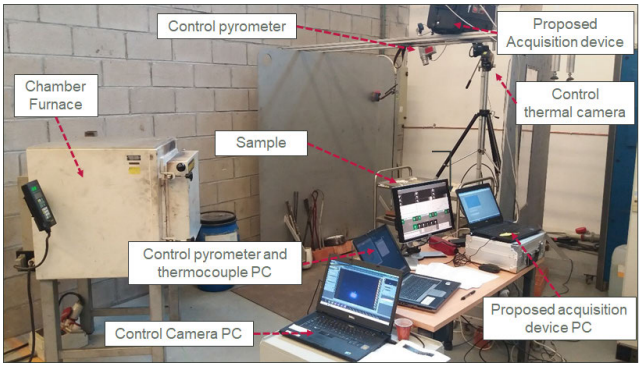

FIGURE 13. Experiment setup. The figure shows the acquisition device mounted on the top part, a control pyrometer and thermal camera, the furnace to heat the sample, the attached thermocouple and the PCs running the acquisition and control software for the different devices.

B. ANALYSIS OF ALUMINA

Alumina ($\alpha - Al_2O_3$) was chosen as a reference material to validate the infrared emissivity measurements performed by the proposed system. Its purity and open porosity were certified by the supplier (McDanel Adv. Ceramic Technologies) to be 99.8% and 0%, respectively. The surface roughness was measured with a profilometer and the average and root mean square values obtained were $R_a = 1.36\,\mu m$ and $R_q = 1.69\,\mu m$, respectively. Then, the infrared reflectance at room temperature was measured (see Fig. 14) to locate the Christiansen wavelength, which was thereby at 9.82 µm, with an emissivity value of 0.99. This value is in very good agreement with the expected one according to the data in the literature [41].

The results of the laboratory emissivity measurements following the approach illustrated in section V-A1 are shown

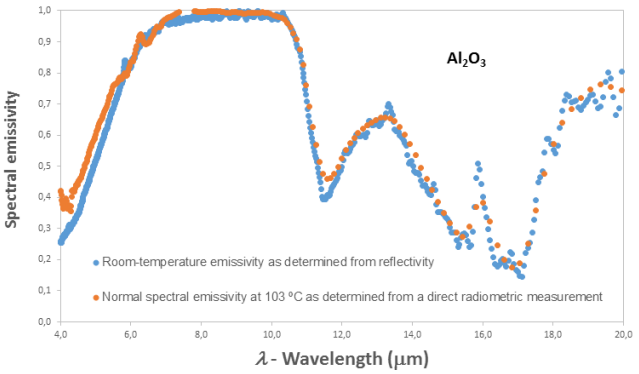

FIGURE 14. Spectral emissivity of the alumina sample measured at room-temperature from reflectivity (blue) and from direct radiometric measurement with the laboratory setup at 103°C (orange).

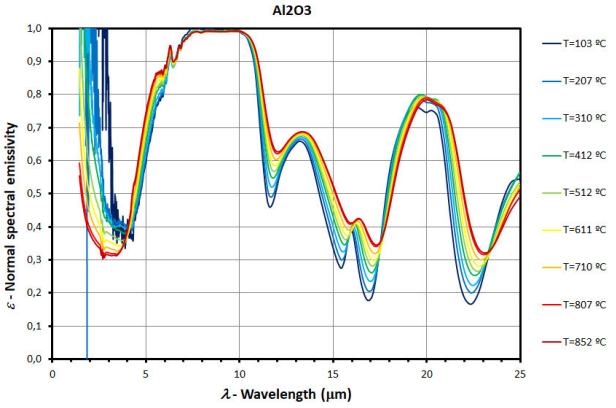

FIGURE 15. Normal spectral emissivity of the Alumina sample as a function of temperature, as measured in laboratory.

in Fig. 15. The shape of the spectra and the thermal evolution are consistent with previous results in the literature and the typical behaviour of dielectric materials [40], [41]. It is important to note that the emissivity values observed below 4 µm will not be considered in this work, because the material becomes semitransparent at those wavelengths and part of the radiation emitted by the heater reaches the detector [40], [45]. The treatment of this effect is out of the scope of the current work. In addition, the feature at 4.18 µm can be explained by the fundamental vibrational mode of CO_2, whereas the H_2O absorption is clearly observed in the $5.5-7.5$ µm range and due to the residual gases present on the optical path. The curve corresponding to the lowest temperature configuration (i.e. 103°C) recorded in this way is also overlaid in Fig. 14, showing good accordance with the room temperature reflectance measurement.

Thereafter, an alumina sample was also analyzed following the industrial setup described in section V-A2. Fig. 16 represents partial results of the algorithm, showing the posterior probability of some of the measured stochastic variables such as sample temperature, spectral emissivity's or H_2O and CO_2 concentrations. Note that we obtain full probability density estimations of the considered probabilistic variables, which constitute a more informative outcome than point estimates obtained from other non Bayesian approaches. Fig. 17 depicts the remaining components of the output of the algorithm. On the top figure, dotted red points show the signal captured by the device after calibration correction. The blue continuous line represents the theoretical radiation from a blackbody at the temperature given by the thermocouple. The green line represents the radiance of an ideal blackbody $L_{bb}(\lambda, \widehat{T}_{bb})$ at the temperature $\widehat{T}_{bb}$ estimated by the algorithm, whereas the black line represents the estimated radiance $\widehat{L}(\lambda, \widehat{T}_{bb})$ of the sample when applying the spectral emissivity $\widehat{\varepsilon}(\lambda, \widehat{T}_{bb})$ estimated by the algorithm to $L_{bb}(\lambda, \widehat{T}_{bb})$. The magenta line represents the calculated spectrum when applying the estimated attenuation caused by CO_2 and H_2O to the spectrum $\widehat{L}(\lambda, \widehat{T}_{bb})$. On the bottom part of the figure we depict spectral the emissivity $\widehat{\varepsilon}(\lambda, \widehat{T}_{bb})$ estimated by the algorithm as defined in eq. 8 and Fig. 10, by composition of the posterior probability estimates of the emissivity's at the anchor wavelengths ε_k.

Fig. 18 shows the comparison between the temperature measured by the thermocouple and the temperature estimated by the proposed system for the alumina at different real temperature values. The comparison yields a Root Mean Square Error (RMSE) of 32.3°C between them and a coefficient of

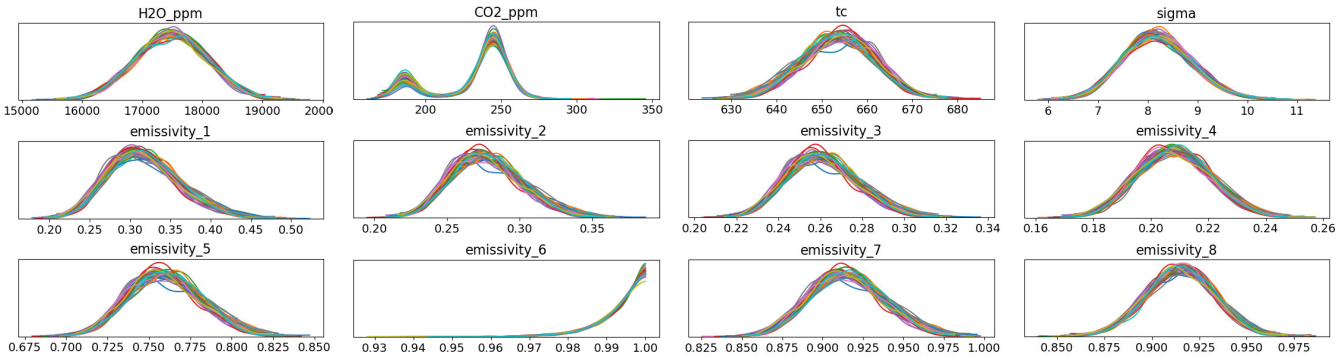

FIGURE 16. Estimated posterior probability of some of the stochastic variables for an alumina sample. Each plot comprises 20 random initializations of the model.

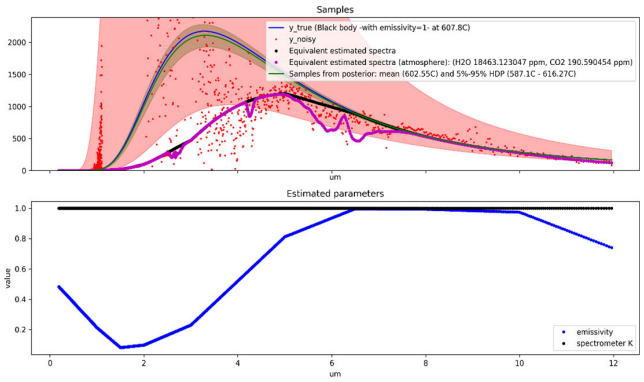

FIGURE 17. Algorithm output for an alumina sample at 607.8°C. Top) Application of probabilistic radiative transfer model to the sample. The blue continuous line represents the theoretical radiation from a blackbody at the temperature given by the thermocouple. The green line represents the radiance of an ideal blackbody $L_{bb}(\lambda, \widehat{T}_{bb})$ at the temperature $\widehat{T}_{bb}$ estimated by the algorithm, whereas the black line represents the estimated radiance $\widehat{L}(\lambda, \widehat{T}_{bb})$ of the sample when applying the spectral emissivity $\widehat{\varepsilon}(\lambda, \widehat{T}_{bb})$ estimated by the algorithm to $L_{bb}(\lambda, \widehat{T}_{bb})$. The magenta line represents the calculated spectrum when applying the estimated attenuation caused by CO_2 and H_2O to the spectrum $\widehat{L}(\lambda, \widehat{T}_{bb})$. Bottom) Emissivities $\widehat{\varepsilon}(\lambda, \widehat{T}_{bb})$ estimated by the algorithm as defined in (8) and Fig. 10.

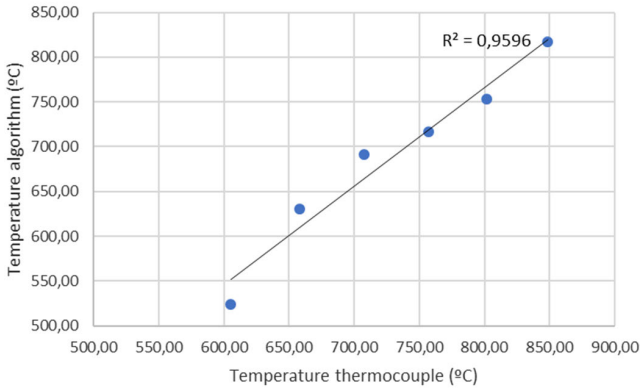

FIGURE 18. Regression graph between the temperature measured by the thermocouple and the temperature estimated by our proposed system and method for the Al_2O_3 sample.

determination $R^2 = 0.96$, thus exhibiting a good correlation across the whole temperature range. Note that the comparatively higher error at the lowest nominal temperatures is consistent with the fact that part of the spectral radiance reaching the system falls below the calibrated range for those temperatures, due to the low emissivity of the sample in such region (see Fig. 17). This range also corresponds to the non-zero transmittance region of the alumina.

Finally, Fig. 19 represents the emissivity's measured under laboratory conditions for the alumina sample at a single temperature setting (see section V-B). The qualitative emissivity behaviour is resembled correctly by the model in the range of 3.6−12.0 µm. The obtained curve is the typical of ceramic materials. From the Christiansen wavelength towards shorter wavelengths, a high-emissivity plateau is observed

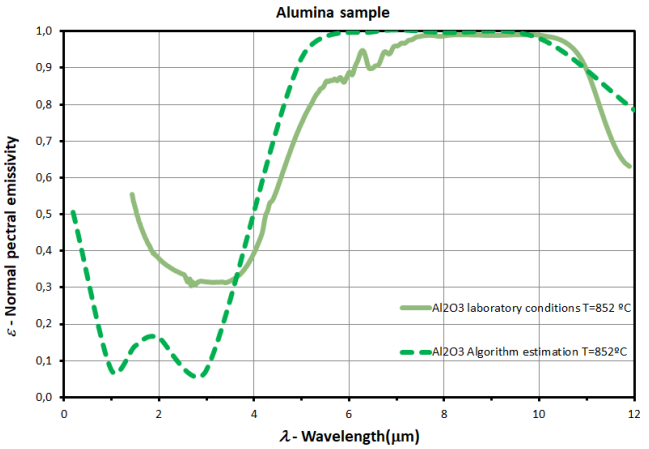

FIGURE 19. Spectral emissivity of the alumina sample determined in laboratory conditions compared to the emissivity estimated by the algorithm under industrial conditions.

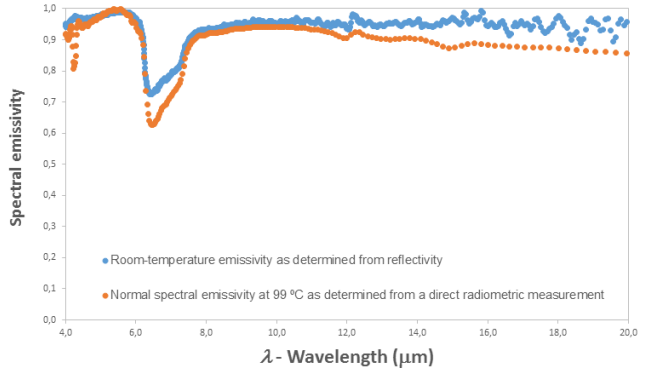

FIGURE 20. Spectral emissivity of the boron nitride sample measured at room-temperature from reflectivity (blue) and from direct radiometric measurement with the laboratory setup at 103°C (orange).

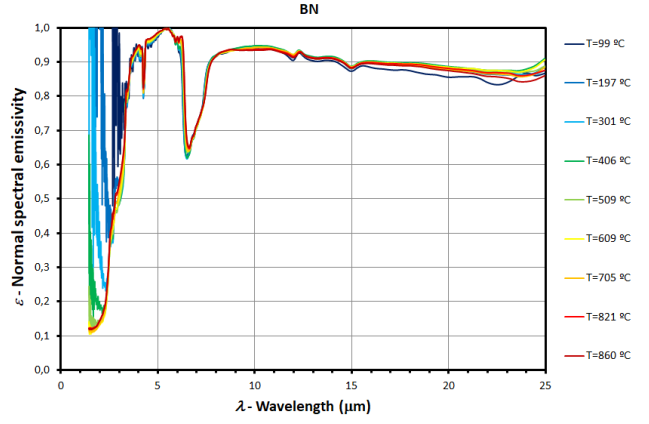

FIGURE 21. Normal spectral emissivity of the hexagonal boron nitride ($h - BN$) sample as a function of temperature, as measured in laboratory.

followed by a steep decrease, whereas towards longer ones the emissivity immediately decreases. For this range it is also observed that there is a more than acceptable quantitative agreement between the algorithm estimation and the

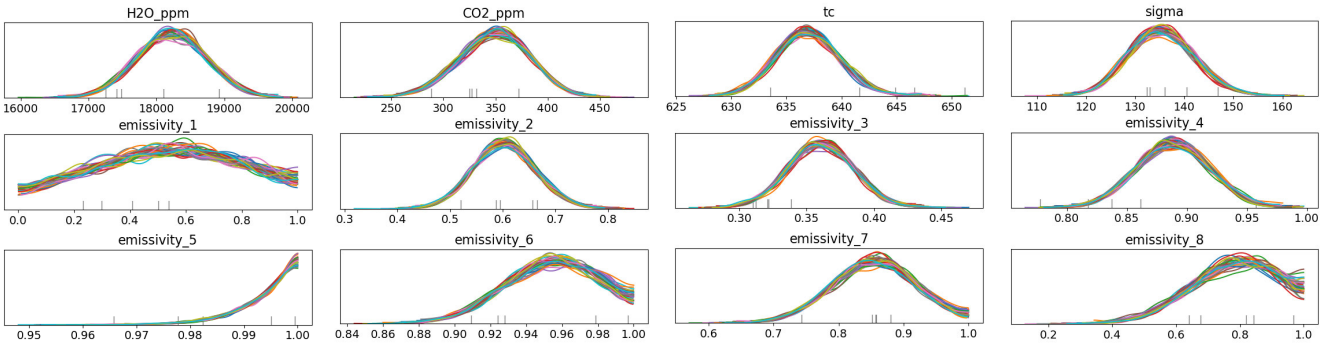

FIGURE 22. Estimated Posterior probability of some of the stochastic variables for a boron nitride sample. Each plot comprises 20 random initializations of the model.

laboratory measurement. Therefore, we can conclude that the proposed system is suitable to adequately estimate the temperature and emissivity of alumina. It is worth mentioning here that below 3.6 µm, both curves differ due to the non-zero transmittance of the sample, and part of the radiation from the heating set is therefore detected by the spectrometer. This semi-transparency effect will not be treated here. Besides, in the laboratory-air measurement tracks of CO_2 and H_2O are evident, while the correction applied in the model appropriately removes these ''artifacts'' from the actual emissivity evolution.

C. ANALYSIS OF BORON NITRIDE

A sample of hexagonal boron nitride ($h-BN$) was used as a reference material complementary to alumina in order to validate infrared emissivity measurements by our system. A sample processed by hot pressing of high-purity powders was purchased from Goodfellow, with a range of porosities of 2-15%. The surface roughness was measured with a profilometer and its average value was $R_a = 0.69$ µm. Finally, the infrared emissivity at room temperature was measured indirectly with an integrating sphere in order to locate the Christiansen wavelength, which was found to be at 5.56 µm, with an emissivity value greater than 0.99 (see Fig. 20), which are in agreement with the data reported in the literature [43]. The results of this measurement are shown in Fig. 21.

The laboratory set-up was again arranged following the description in section V-A1 and the same procedure as with the alumina sample was used. The results of the laboratory emissivity measurements (shown in Fig. 21 for the 99-860°C range and in Fig. 20 for the 99°C case for direct comparison with the reflectivity-based measurement at room-temperature) were again found to be consistent with the literature and the typical behaviour of dielectric materials in terms of shape of the spectra and the evolution as a function of the temperature. As a difference with the measurement acquired from the sample of alumina, the plateau around the Christiansen wavelength is much shorter with decreasing emissivity towards both sides. Of course, as these measurements were also performed under laboratory air the absorption peaks corresponding to $CO2$ and H_2O are also visible.

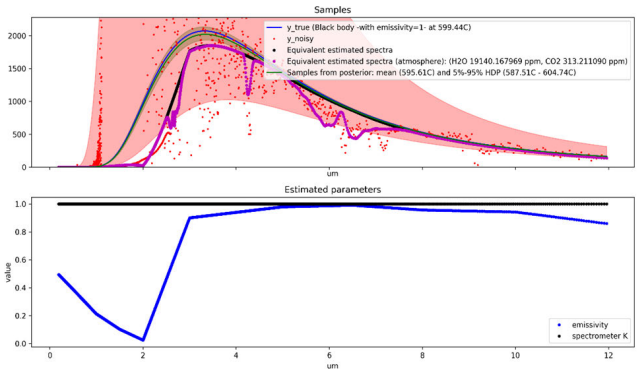

FIGURE 23. Algorithm output for an boron nitride sample at 599.44.8°C. Top) Application of probabilistic radiative transfer model to the sample. The blue continuous line represents the theoretical radiation from a blackbody at the temperature given by the thermocouple. The green line represents the radiance of an ideal blackbody $L_{bb}(\lambda, \hat{T}_{bb})$ at the temperature $\hat{T}_{bb}$ estimated by the algorithm, whereas the black line represents the estimated radiance $\hat{L}(\lambda, \hat{T}_{bb})$ of the sample when applying the spectral emissivity $\hat{\varepsilon}(\lambda, \hat{T}_{bb})$ estimated by the algorithm to $L_{bb}(\lambda, \hat{T}_{bb})$. The magenta line represents the calculated spectrum when applying the estimated attenuation caused by CO_2 and H_2O to the spectrum $\hat{L}(\lambda, \hat{T}_{bb})$. Bottom) Emissivities $\hat{\varepsilon}(\lambda, \hat{T}_{bb})$ estimated by the algorithm as defined in (8) and Fig. 10.

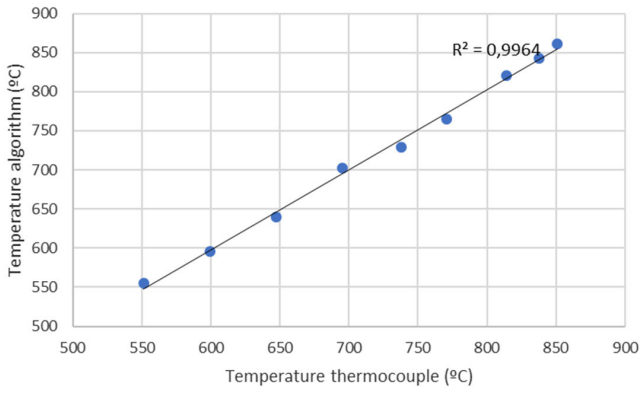

FIGURE 24. Regression graph between the temperature measured by the thermocouple and the temperature estimated by our proposed system and method for the *BN* sample.

Another particular feature for $h-BN$ in the range of interest for this work, i.e. from 4 to 12 µm in wavelength, is the

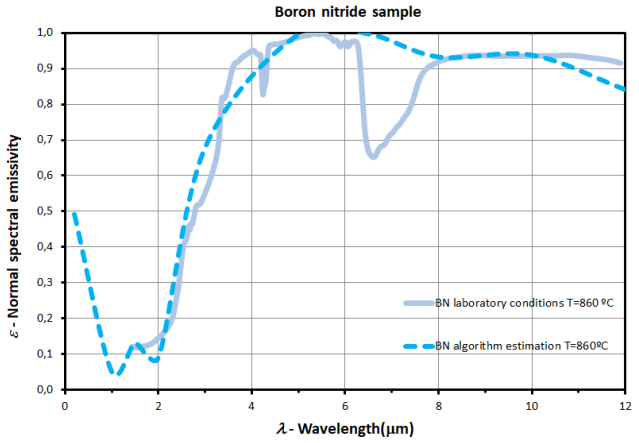

FIGURE 25. Boron nitride emissivity determined in laboratory conditions compared with the emissivity estimated by the algorithm under industrial conditions.

wide peak observed between 6 and 8 µm, what corrresponds to an infrared active phonon (for details see [43]). Finally, semi-transparency effects for $h-BN$ are not so significant as for alumina below 4 µm, leading to reliable emissivity data down to 2 µm.

For the industrial conditions measurement, the same configuration and procedure as with the alumina experiment was followed, stopping the experiment at 500°C, once the radiance signal became noisy for our system. Fig. 22 shows the posterior probabilities of some of the stochastic variables estimated of the algorithm whereas, Fig. 23 presents the algorithm's estimations for a boron nitride sample at 599.44°C, following the notation from Fig. 17.

The temperature estimation obtained for this sample shows an even better correlation across the whole range with the thermocouple measurements than in the case of the alumina, as can be seen in Fig. 24 (RMSE= 5.69°C, $R^2 = 0.996$). Finally, (Fig. 25) compares the emissivity's measured under laboratory conditions with those estimated under industrial conditions for a fixed temperature value of 852°C. It can be appreciated that there is a quite good qualitative and quantitative agreement between both in the $2-12$ µm range, except for the region corresponding to the active infrared phonon (6-8 µm) that is removed from the model. This phenomenon is beyond the scope of the current work.

Furthermore, we can observe that the CO_2 (at 4.2 µm) and H_2O (at 5.8 µm and 6.5 µm) absorptions present in the laboratory measurements are adequately treated by our algorithm and eliminated from the emissivity, thus giving a correct spectra of the actual emissivity.

VI. CONCLUSION

In this work we presented, to our knowledge, the first capturing device that is able to simultaneously estimate the spectral emissivity and temperature of a hot emissive material under real steel factory conditions. The presented device is capable of capturing $0.2-12$ µm range radiance signal at up to 20 m away from the sample, over a 12 mm diameter spot. The device allows for in-situ calibration making use of a stabilized calibration lamp. The system is accompanied by a probabilistic algorithm that is able to produce simultaneous full probability density estimates of the sample temperature and spectral emissivity at different wavelengths, as well as the global concentration of H_2O and CO_2 along the optical path. All these parameters are seamlessly predicted by a Markov Chain Montecarlo-based estimation algorithm as the ones that provide the best explanation for the captured data.

We showed that, by analyzing the radiance between $0.2-12$ µm, we were capable of estimating the temperature of alumina and boron nitride samples in a range of 600-1000°C with an RMSE of 32.3°C and 5.69°C, respectively. Spectral emissivity was calculated accurately and the effect of H_2O and CO_2 absorption was also estimated and discounted from the measurement.

These results pave the path for future attempts to estimate the slag composition on the electric arc furnace based on the analysis of the predicted emissivity values.

ACKNOWLEDGMENT

(Artzai Picon and Aitor Alvarez-Gila contributed equally to this work.)

REFERENCES

[1] Worldsteel Association. *Steel Facts 2019*. Accessed: 2020. [Online]. Available: https://www.worldsteel.org/en/dam/jcr:ab8be93e-1d2f-4215-9143-4eba6808bf03/20190207_steelFacts.pdf

[2] H. Köchner, "Sensors and measurement techniques for process control," in *Proc. Workshop Elect. Arc Furnace, State-Art RFCS-Supported Projects*, 2015.

[3] M. Blachnik, K. Mączka, and T. Wieczorek, "A model for temperature prediction of melted steel in the electric arc furnace (EAF)," in *Proc. Int. Conf. Artif. Intell. Soft Comput.* Berlin, Germany: Springer, 2010, pp. 371–378.

[4] A. Vicente, A. Picon, J. A. Arteche, M. Linares, A. Velasco, and J. A. Sainz, "Magnetic field-based arc stability sensor for electric arc furnaces," *Measurement*, vol. 151, Feb. 2020, Art. no. 107134.

[5] A. Picon, A. Vicente, S. Rodriguez-Vaamonde, J. Armentia, J. A. Arteche, and I. Macaya, "Ladle furnace slag characterization through hyperspectral reflectance regression model for secondary metallurgy process optimization," *IEEE Trans. Ind. Informat.*, vol. 14, no. 8, pp. 3506–3512, Aug. 2018.

[6] H. Pauna, M. Aula, J. Seehausen, J.-S. Klung, M. Huttula, and T. Fabritius, "Optical emission spectroscopy as an online analysis method in industrial electric arc furnaces," *Steel Res. Int.*, vol. 91, no. 11, Nov. 2020, Art. no. 2000051.

[7] A. Vicente, A. Picon, J. A. Arteche, M. Linares, A. Velasco, and J. A. Sainz, "Magnetic field-based arc stability sensor for electric arc furnaces," *Measurement*, vol. 151, Feb. 2020, Art. no. 107134.

[8] S. Bohnes, V. Scherer, S. Linka, M. Neuroth, and H. Brüggemann, "Spectral emissivity measurements of single mineral phases and ash deposits," in *Proc. ASME Summer Heat Transf. Conf.*, Jan. 2005, pp. 175–182.

[9] R. J. Lee, M. S. Ramsey, and P. L. King, "Development of a new laboratory technique for high-temperature thermal emission spectroscopy of silicate melts," *J. Geophys. Res., Solid Earth*, vol. 118, no. 5, pp. 1968–1983, 2013.

[10] S. Tsuda, T. Okazaki, and A. Gwosdz, "Proposal for predictive expressions of emissivity spectra for powdery coal ash," *J. Power Energy Syst.*, vol. 6, no. 3, pp. 360–377, 2012.

[11] T. J. Moore, D. P. Cundick, M. R. Jones, D. R. Tree, R. D. Maynes, and L. L. Baxter, "*In situ* measurements of the spectral emittance of coal ash deposits," *J. Quant. Spectrosc. Radiat. Transf.*, vol. 112, no. 12, pp. 1978–1986, Aug. 2011. [Online]. Available: http://www.sciencedirect.com/science/article/pii/S0022407311001713

[12] S. Linka, S. Wirtz, and V. Scherer, "Spectral thermal radiation characteristics of coal ashes and slags: Influence of chemical composition and temperature," in *Proc. ASME Heat Transf. Summer Conf.*, Las Vegas, NV, USA, Jan. 2003, pp. 33–39.

[13] T. Paloposki and L. Liedquist, "Steel emissivity at high temperatures," VTT Tech. Res. Centre Finland, Espoo, Finland, 2005.

[14] S. Rego-Barcena, R. Saari, R. Mani, S. El-Batroukh, and M. J. Thomson, "Real time, non-intrusive measurement of particle emissivity and gas temperature in coal-fired power plants," *Meas. Sci. Technol.*, vol. 18, no. 11, p. 3479, Nov. 2007. [Online]. Available: http://iopscience.iop.org/0957-0233/18/11/031

[15] S. R. Barcena, "A passive mid-infrared sensor to measure real-time particle emissivity and gas temperature in coal-fired boilers and steelmaking furnaces," Ph.D. dissertation, Univ. Toronto, Toronto, ON, Canada, 2008.

[16] G. H. Richards, J. N. Harb, L. L. Baxter, S. Bhattacharya, R. P. Gupta, and F. T. Wall, "Radiative heat transfer in pulverized-coal-fired boilers—Development of the absorptive/reflective character of initial ash deposits," in *Proc. Symp. Int. Combustion*, 1994, vol. 25, no. 1, pp. 511–518. [Online]. Available: http://www.sciencedirect.com/science/article/pii/S0082078406806806

[17] J. R. Howell, "The Monte Carlo method in radiative heat transfer," *J. Heat Transf.*, vol. 120, no. 3, pp. 547–560, Aug. 1998, doi: 10.1115/1.2824310.

[18] P. Heasler, C. Posse, J. Hylden, and K. Anderson, "Nonlinear Bayesian algorithms for gas plume detection and estimation from hyper-spectral thermal image data," *Sensors*, vol. 7, no. 6, pp. 905–920, Jun. 2007. [Online]. Available: http://www.mdpi.com/1424-8220/7/6/905

[19] C. Dickinson, H. K. Eriksen, A. J. Banday, J. B. Jewell, K. M. Górski, G. Huey, C. R. Lawrence, I. J. O'Dwyer, and B. D. Wandelt, "Bayesian component separation and cosmic microwave background estimation for the five-year WMAP temperature data," *Astrophys. J.*, vol. 705, no. 2, p. 1607, 2009. [Online]. Available: http://stacks.iop.org/0004-637X/705/i=2/a=1607

[20] H. K. Eriksen, J. B. Jewell, C. Dickinson, A. J. Banday, K. M. Górski, and R. C. Lawrence, "Joint Bayesian component separation and CMB power spectrum estimation," *Astrophys. J.*, vol. 676, no. 1, p. 10, 2008. [Online]. Available: http://stacks.iop.org/0004-637X/676/i=1/a=10

[21] P. Rosales, C. Blanco, M. Flores, R. Pareja, A. Revuelta, and F. Marquez, "Comparison between the 'grey body emissivity' and 'Bayesian inference' methods to retrieve temperature and emissivity from FTIR spectroradiometer measurements," *Proc. SPIE*, vol. 7834, Oct. 2010, Art. no. 783411.

[22] C. Berrett, G. P. Williams, T. Moon, and J. Gunther, "A Bayesian nonparametric model for temperature-emissivity separation of long-wave hyperspectral images," *Technometrics*, vol. 56, no. 2, pp. 200–211, Apr. 2014, doi: 10.1080/00401706.2013.869262.

[23] P. Dash, F.-M. Göttsche, F.-S. Olesen, and H. Fischer, "Land surface temperature and emissivity estimation from passive sensor data: Theory and practice-current trends," *Int. J. Remote Sens.*, vol. 23, no. 3, pp. 2563–2594, 2002, doi: 10.1080/01431160110115041.

[24] F. Jacob, F. Petitcolin, T. Schmugge, É. Vermote, A. French, and K. Ogawa, "Comparison of land surface emissivity and radiometric temperature derived from MODIS and ASTER sensors," *Remote Sens. Environ.*, vol. 90, no. 2, pp. 137–152, Mar. 2004. [Online]. Available: http://www.sciencedirect.com/science/article/pii/S0034425703003699

[25] J. A. Morgan, "Bayesian estimation for land surface temperature retrieval: The nuisance of emissivities," *IEEE Trans. Geosci. Remote Sens.*, vol. 43, no. 6, pp. 1279–1288, Jun. 2005.

[26] J. A. Morgan, "A Bayesian estimator for linear calibration error effects in thermal remote sensing," *IEEE Geosci. Remote Sens. Lett.*, vol. 3, no. 1, pp. 117–119, Jan. 2006. [Online]. Available: http://arxiv.org/abs/physics/0501087

[27] J. A. Morgan, "Comparison of Bayesian land surface temperature algorithm performance with Terra MODIS observations," *Int. J. Remote Sens.*, vol. 32, no. 23, pp. 8139–8159, Dec. 2011, doi: 10.1080/01431161.2010.532824.

[28] A. Barducci, D. Guzzi, C. Lastri, V. Nardino, I. Pippi, and V. Raimondi, "Emissivity spectra estimated with the MaxEnTES algorithm," *Proc. SPIE*, vol. 9241, Oct. 2014, Art. no. 92411P.

[29] A. Barducci, D. Guzzi, C. Lastri, P. Marcoionni, V. Nardino, and I. Pippi, "Emissivity and temperature assessment using a maximum entropy estimator: Structure and performance of the MaxEnTES algorithm," *IEEE Trans. Geosci. Remote Sens.*, vol. 53, no. 2, pp. 738–751, Feb. 2015.

[30] J. Liu, H. Li, J. Wang, H. Li, L. Yin, and Z. Zhang, "Inversion of emissivity spectrum and temperature in the TIR waveband based on the maximum entropy," *Infr. Phys. Technol.*, vol. 72, pp. 179–190, Sep. 2015. [Online]. Available: http://www.sciencedirect.com/science/article/pii/S135044951500167X

[31] S. Sonoda, N. Murata, H. Hino, H. Kitada, and M. Kano, "A statistical model for predicting the liquid steel temperature in ladle and tundish by bootstrap filter," *ISIJ Int.*, vol. 52, no. 6, pp. 1086–1091, 2012.

[32] M. Wiecek, R. Strakowski, B. Wiecek, R. Olbrycht, T. Swiątczak, W. Wittchen, and M. Borecki, "Estimation of steel slag parameters using thermal imaging and neural networks classification," in *Proc. 10th Int. Conf. Quant. InfraRed Thermogr. (QIRT)*. Quebec City, QC, Canada: Laval Univ., 2010, pp. 1–5.

[33] C. J. Willers, *Electro-Optical System Analysis and Design: A Radiometry Perspective*. Bellingham, WA, USA: SPIE Press, Apr. 2013.

[34] I. E. Gordon *et al.*, "The HITRAN2016 molecular spectroscopic database," *J. Quant. Spectrosc. Radiat. Transf.*, vol. 203, pp. 3–69, Dec. 2017.

[35] R. V. Kochanov, I. E. Gordon, L. S. Rothman, P. Wcisło, C. Hill, and J. S. Wilzewski, "HITRAN application programming interface (HAPI): A comprehensive approach to working with spectroscopic data," *J. Quant. Spectrosc. Radiat. Transf.*, vol. 177, pp. 15–30, Jul. 2016.

[36] C. C. Borel, "Surface emissivity and temperature retrieval for a hyperspectral sensor," in *Proc. IEEE Int. Geosci. Remote Sens. Symp. (IGARSS)*, vol. 1, Jul. 1998, pp. 546–549.

[37] J. Salvatier, T. V. Wiecki, and C. Fonnesbeck, "Probabilistic programming in Python using PyMC3," *PeerJ Comput. Sci.*, vol. 2, p. e55, Apr. 2016.

[38] A. Gelman, "Prior distributions for variance parameters in hierarchical models (comment on article by Browne and Draper)," *Bayesian Anal.*, vol. 1, no. 3, pp. 515–534, Sep. 2006.

[39] M. D. Homan and A. Gelman, "The no-U-turn sampler: Adaptively setting path lengths in Hamiltonian Monte Carlo," *J. Mach. Learn. Res.*, vol. 15, no. 1, pp. 1593–1623, Jan. 2014.

[40] I. G. de Arrieta, T. Echániz, R. Fuente, J. M. Campillo-Robles, J. M. Igartua, and G. A. López, "Updated measurement method and uncertainty budget for direct emissivity measurements at the university of the basque country," *Metrologia*, vol. 57, no. 4, Jul. 2020, Art. no. 045002.

[41] B. Rousseau, J. F. Brun, D. D. S. Meneses, and P. Echegut, "Temperature measurement: Christiansen wavelength and blackbody reference," *Int. J. Thermophys.*, vol. 26, no. 4, pp. 1277–1286, Jul. 2005.

[42] O. Rozenbaum, D. De Sousa Meneses, and P. Echegut, "Texture and porosity effects on the thermal radiative behavior of alumina ceramics," *Int. J. Thermophys.*, vol. 30, no. 2, pp. 580–590, Apr. 2009.

[43] I. G. de Arrieta, T. Echániz, R. Fuente, L. del Campo, D. De Sousa Meneses, G. A. López, and M. J. Tello, "Mid-infrared optical properties of pyrolytic boron nitride in the 390–1050 °C temperature range using spectral emissivity measurements," *J. Quant. Spectrosc. Radiat. Transf.*, vol. 194, pp. 1–6, Jun. 2017.

[44] T. Echániz, R. B. Pérez-Sáez, and M. J. Tello, "IR radiometer sensitivity and accuracy improvement by eliminating spurious radiation for emissivity measurements on highly specular samples in the 2–25 μm spectral range," *Measurement*, vol. 110, pp. 22–26, Nov. 2017.

[45] S. Jeon, S.-N. Park, Y. S. Yoo, J. Hwang, C.-W. Park, and G. W. Lee, "Simultaneous measurement of emittance, transmittance, and reflectance of semitransparent materials at elevated temperature," *Opt. Lett.*, vol. 35, no. 23, pp. 4015–4017, Dec. 2010.

ARTZAI PICON received the M.Eng. degree in industrial engineering, in 2002, the M.Res. degree in automatics electronics and control, in 2005, and the European Ph.D. degree, in 2009. In 2002, he started working as a Researcher at Robotiker, where he was involved in over 50 research and turnkey computer vision projects. In 2007, he was with the Centre for Image Processing and Analysis (CIPA). He has published multiple articles and holds several patents. In 2002, he received the Best M.Eng. Final Project Award from Accenture Company for the implementation of a facial recognition system and the ONCE International Research and Development Award in New Technologies for the Blind and Visually Impaired, in 2006. In 2011, the industrial application of his thesis developments received the 3rd EARTO's Award on Innovation. In 2011, he joins Tecnalia Research and Innovation performing research and management tasks on the computer vision field. In 2014, he received the 1st EARTO's Award on Innovation. He is currently a reviewer of different journals related to machine vision and artificial intelligence.

AITOR ALVAREZ-GILA received the M.Sc. degree in telecommunications engineering from The University of the Basque Country. He is currently pursuing the Ph.D. degree in deep learning techniques Learning and Machine Perception Team (LAMP), Computer Vision Centre (CVC), Universitat Autònoma de Barcelona (UAB). After working for three years as a technology consultant in Madrid and London (Accenture, Management Solutions), from 2008 to 2010, he completed the Erasmus Mundus Master CIMET (Colour in Informatics and Media Technology) in machine vision and colour science, visiting the Universities of Granada, Saint-Etienne, GjØvik and Amsterdam. Since 2010, he has been a Researcher with the Tecnalia's Computer Vision Group. He has collaborated in projects on image processing for underwater and adverse weather conditions, hyperspectral imaging, 3-D reconstruction and image understanding for the biomedical, agricultural, packaging, and steel industries. He is a member of the Learning and Machine Perception Team (LAMP), Computer Vision Centre (CVC), Universitat Autònoma de Barcelona (UAB). He has published several papers in Q1 journals and top-tier conferences and holds multiple patents. In 2014, he received the 1st EARTO Award on Innovation for the development of a histopathological image retrieval system. He is a reviewer of various journals on computer vision and signal processing.

JOSE ANTONIO ARTECHE received the B.Eng. degree in electronic engineering, in 1984, the M.Eng. degree in industrial engineering, in 1989, and the M.Sc. degree in systems engineering and process control. In 1990, he started working as a Researcher at Robotiker and participated in projects related to information and communication technologies. In 2011, he joined Tecnalia Research and Innovation performing tasks from research to management.

GABRIEL A. LÓPEZ received the degree in chemical engineering from the National University of Comahue, Argentina, and the Ph.D. degree in materials science from the Max Planck Institute for Metals Research, Stuttgart, Germany. Then, through a Marie Curie Fellowship, he moved to the University of the Basque Country UPV/EHU, Bilbao, Spain, where he broadened his expertise on electron microscopy and physical metallurgy. Since July 2016, he has been an Associate Professor with UPV/EHU and in charge of the Research Group on Thermophysical Properties of Materials. He is the Vice-Dean for Students Affairs of the Faculty of Science and Technology, UPV/EHU. He has published more than 50 indexed articles (H=15), participated in multiple research projects, given several invited talks in international conferences. He is a member of the Editorial Board of a *JCR* journal and a reviewer for various journals.

ASIER VICENTE received the B.Eng. degree in civil engineering in 2002, the M.Eng. degree (Hons.) in material engineering from the School of engineering of Bilbao, and the M.Sc. degree in industrial technologies by UNED, in 2016 and Ph.D. degree, in 2020. In 2002, he was a steel mill shift manager at ArcelorMittal Sestao. In 2010, he moved to Arcelor Basque Country Research and Development Center. He currently works as a principal investigator in the electric arc furnace and raw materials area, leading numerous projects in this area. He participates as an Active Member in several global technical committees within ArcelorMittal, such as "ArcelorMittal Global Expert Technical Committee" in the processes of electric arc furnace and secondary metallurgy, "AM Measurement & Control Cluster", and optical temperature and raw materials and molten phases characterization community of practices (acting as global coordinator of the latter).